

## Research Article

# Cochlear Fluid Spaces and Structures of the Gerbil High-Frequency Region Measured Using Optical Coherence Tomography (OCT)

NAM HYUN CHO<sup>1,2</sup>, HAOBING WANG<sup>1,2</sup>, AND SUNIL PURIA<sup>1,2,3</sup> 

<sup>1</sup> Department of Otolaryngology–Head and Neck Surgery, Harvard Medical School, Boston, MA 02114, USA

<sup>2</sup> Eaton-Peabody Laboratories, Massachusetts Eye and Ear, Boston, MA 02114, USA

<sup>3</sup> Speech and Hearing Bioscience and Technology Program, Harvard University, Cambridge, MA 02138, USA

Received: 19 May 2021; accepted: 4 January 2022; Online publication: 22 February 2022

## ABSTRACT

Since it has been difficult to directly observe the morphology of the living cochlea, our ability to infer the mechanical functioning of the living ear has been limited. Nearly all our knowledge about cochlear morphology comes from postmortem tissue that was fixed and processed using procedures that possibly distort the structures and fluid spaces of the organ of Corti. In this study, optical coherence tomography was employed to obtain volumetric images of the high-frequency hook region of the gerbil cochlea, as viewed through the round window, with far better resolution capability than had been possible before. The anatomical structures and fluid spaces of the organ of Corti were segmented and quantified *in vivo* and over a 90-min postmortem period. We find that the arcuate-zone and pectinate-zone widths change very little postmortem. The volume of the scala tympani between the round-window membrane and basilar membrane and the volume of the inner spiral sulcus decrease in the first 60-min postmortem. While textbook drawings of the mammalian organ of Corti and cortilymph prominently depict the tunnel of Corti, the outer tunnel is typically missing. This is likely because textbook drawings are typically made from images obtained by histological methods. Here, we show that the outer tunnel is nearly twice as big as the tunnel of Corti or the space of Nuel. This larger outer tunnel fluid space could have a substantial,

little-appreciated effect on cochlear micromechanics. We speculate that the outer tunnel forms a resonant structure that may affect reticular-lamina motion.

**Keywords:** optical coherence tomography, gerbil, cochlea, organ of corti, cortilymph, cochlear mechanics

## INTRODUCTION

A touchstone of biological research is the notion that structure determines function. In the auditory system, hearing function is closely associated with the intricate structure of the organ of Corti (OoC), the sensory epithelium within the spiral-shaped fluid-filled cochlea of the inner ear. The OoC itself is attached to the basilar membrane (BM), which mechanically partitions the cochlear fluid space as it runs along the length of the spiral from the high-frequency basal hook region (Fig. 1a–c) to the low-frequency apical end of the cochlea.

While there has been rapid progress in the use of optical coherence tomography (OCT) for *in vivo* vibrometry measurements of cochlear function, little attention has been paid to the morphology of the OoC in the living cochlea. Nearly all of our knowledge about OoC cellular and extracellular structure comes from histologically processed, postmortem (PM) cochleae that have been fixed, decalcified, sliced, stained, and imaged with light or electron microscopy (Lim and Anniko 1985; Plassmann et al. 1987; O'Malley et al. 2009). Alternate approaches include hemicochlea preparation and confocal microscopy using

Correspondence to: Sunil Puria · Department of Otolaryngology–Head and Neck Surgery · Harvard Medical School · Boston, MA, 02114, USA. email: Sunil\_Puria@meei.harvard.edu

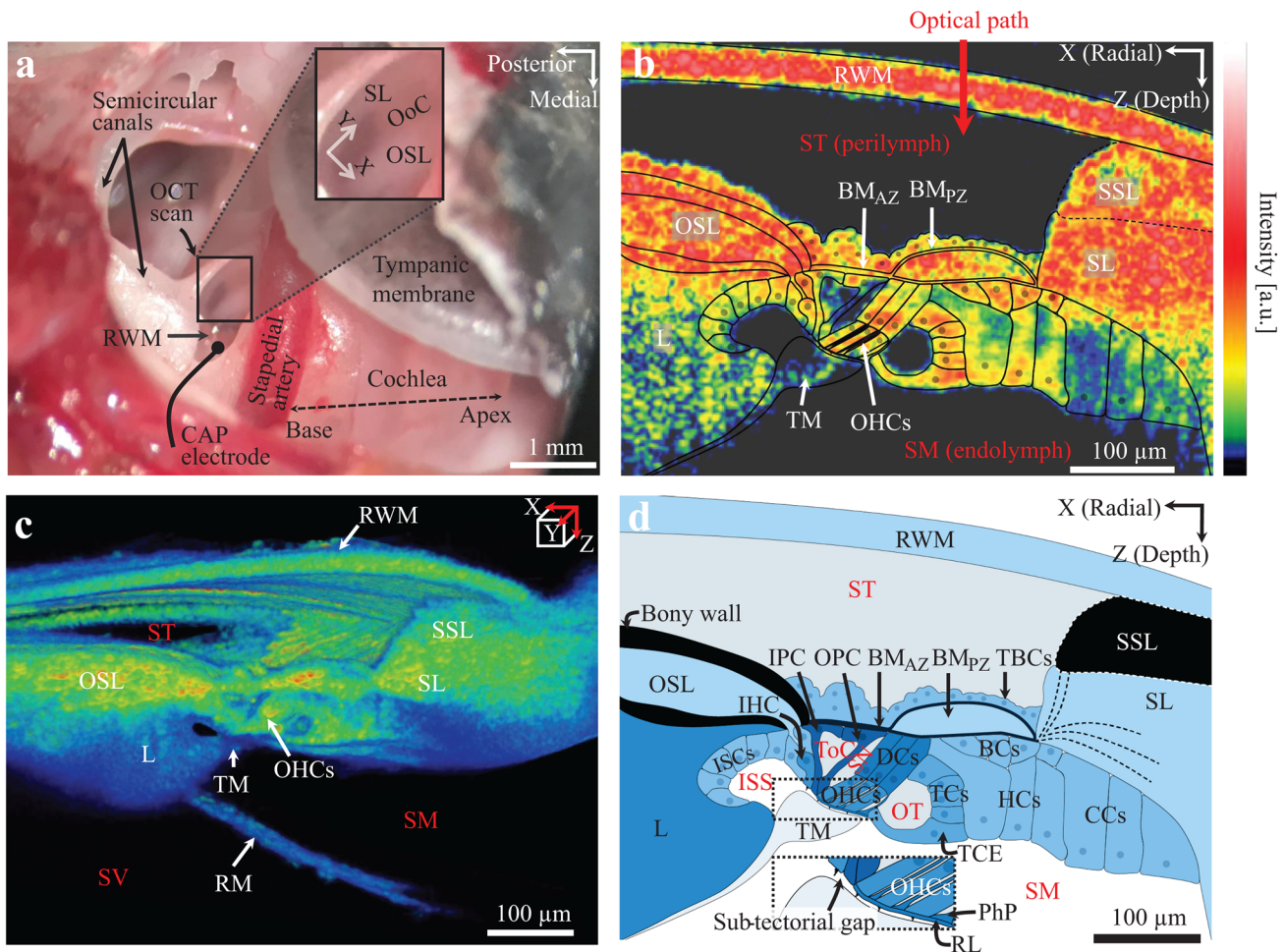


**FIG. 1.** The anatomy of the gerbil ear. **a** A photograph of a surgically opened right middle ear (from animal #188R) shows the region of the round-window membrane (RWM; black rectangle) through which the organ of Corti (OoC) in the “hook region” of the cochlea (enlarged inset image) can be imaged using optical coherence tomography (OCT). In the inset image, the X (approximately radial) and Y (approximately longitudinal) axes indicate the OCT scanning directions for 2D cross-section and 3D volume measurements, based on left-hand coordinates, with the Z (depth) direction pointing into the page. An electrode used for compound action potential (CAP) recordings was typically placed in the niche near the RWM. **b** A 2D cross-sectional OCT image (from animal #191) overlaid with a line drawing of the cells and fluid spaces inferred from the image. (Additional abbreviations in panels **b–d** are defined below). **c** A stack of 2D OCT-imaged cross sections (also from animal #191), from ~0.1 to 1.1 mm from the basal end of the cochlea, forms a 3D volumetric representation of the OoC (Movie [SI-1](#) steps through the image stack sequentially). **d** A labeled cross-sectional

drawing of a representative OoC as imaged through the RWM, based on the 2D OCT image in **b**. Cortilymph-filled spaces include the tunnel of Corti (ToC), space of Nuel (SN), outer tunnel (OT), and the spaces between the outer hair cells (OHCs). The dashed lines in the spiral-ligament (SL) region have been added to represent the continuation of the basilar-membrane (BM) collagen fibers. The enlarged inset shows details of the sub-tectorial gap. Other abbreviations: BCs, Boettcher cells;  $BM_{AZ}$  and  $BM_{PZ}$ , arcuate zone and pectinate zone of the basilar membrane, respectively; CCs, Claudius cells; DCs, Deiters’ cells; HCs, Hensen’s cells; IHC, inner hair cell; IPC and OPC, inner and outer pillar cell, respectively; ISCs, inner-sulcus cells; L, limbus; OSL, osseous (primary) spiral lamina; PhP, phalangeal process; RL, reticular lamina; RM, Reissner’s membrane; SSL, (osseous) secondary spiral lamina; TBCs, tympanic border cells; TCs, tectal cells; TCE, tectal-cell extension; ST, scala tympani; SM, scala media; SV, scala vestibuli; and ISS, inner spiral sulcus.

whole-mount tissue, but they also use PM tissue (Edge et al. 1998; Hardie et al. 2004). The shortcomings of these methods include an uncertain relationship to the living anatomy and unknown preparation-related distortions of the fluid spaces and OoC structures. These unknowns have limited our ability to deduce function from anatomy.

Knowledge of the OoC fluid spaces and surrounding structures is important for a full understanding of the

active and passive cochlea. The OoC fluid spaces are defined to contain the following: (1) the inner spiral sulcus (ISS), which is connected to the sub-tectorial fluid space; and (2) the cortilymph space, consisting of the tunnel of Corti (ToC), the space of Nuel (SN), the fluid space around the outer hair cells (OHCs), and the outer tunnel (OT; Fig. 1d). However, most of these fluid spaces are typically absent in histological images of the high-frequency

hook region. While many studies have focused on OoC structures (Plassmann et al. 1987; Souter et al. 1995; Hu et al. 1999; Richter et al. 2000; Spicer et al. 2003), less attention has been paid to OoC fluid spaces, and particularly, the ISS and OT. The OoC width is known to be important for frequency-to-place mapping of sound, but it has only been measured from PM tissue. To characterize the in vivo OoC structures and fluid spaces, anatomical methods that work in living animals are needed.

OCT is an optical imaging modality with micron-scale axial and lateral resolutions that enables non-invasive and non-destructive imaging of 2D cross sections and 3D volumes of unlabeled biological tissue using backscattered near-infrared broadband light (Huang et al. 1991). Micro-OCT ( $\mu$ OCT) technology has been used to image guinea-pig temporal bones with sub-micron-level axial and lateral resolutions, allowing visualization of the cochlear micro-anatomy at a cellular level (Iyer et al. 2016). While the resolutions of  $\mu$ OCT images are the highest yet achieved for OCT imaging, these measurements have been from ex vivo cochleae that were chemically fixed. In this study, we used a commercial OCT system to collect in vivo 2D images of the gerbil OoC fluid spaces and surrounding structures in the gerbil basal-turn hook region. The images were made through the intact round-window membrane (RWM; Fig. 1a–c), with axial and lateral resolutions (in water) of  $\sim 1.4$  and  $\sim 1.95$   $\mu$ m, respectively. In addition, multiple 3D-volume scans, each with a depth of  $\sim 0.3$  mm, were obtained at different focal depths and concatenated to obtain a 1–1.2-mm volume depth (Fig. 1c; Movie SI-1). We obtained images during the in vivo state over the course of 1 h, and over an additional 90 min following death. This procedure allowed us to image the OoC structures while the animal was alive, and to then observe changes in the dimensions and orientations of the OoC structures and fluid spaces at different PM-interval states.

The BM width; OoC height and area; and fluid volumes of the ISS, ToC, SN, and OT, as well as the scala tympani (ST) region between the RWM and BM, were segmented to test the hypothesis that they change with animal state. To directly compare the OCT-based morphometry against morphometry obtained using histological methods, we processed a subset of ears using an aldehyde fixation followed by celloidin embedding and serial sectioning, an approach reported to best preserve the delicate architecture of the inner-ear epithelia (O'Malley et al. 2009).

## MATERIALS AND METHODS

### Animals and Surgical Approach

This study was approved by the Institutional Animal Care and Use Committee (IACUC) at Massachusetts Eye and Ear (MEE). Healthy Mongolian gerbils, *Meriones unguiculatus*, ( $N=14$ , aged 5–32 weeks, weight range 60–111 g)

of either sex (7 males, 7 females) were used for this study. In vivo OCT results are reported for the five left ears from which OCT volume scans were obtained, PM OCT results are reported for three of those five ears, and histology results are reported for one of those five ears and its opposite ear. Histology results from both ears of one additional animal are also reported.

All surgical procedures, including anesthesia, were performed in a private surgery room near the sound-proof chamber in which the experiments were conducted. The initial anesthesia was induced by an intraperitoneal (IP) injection of sodium pentobarbital (70 mg/kg), followed by a subcutaneous (SQ) injection of acepromazine (1 mg/kg) mixed with atropine (0.06 mg/kg). Lidocaine (1%) with epinephrine (1:100,000) was applied topically to the skin over the top of the skull and around the left ear. Puralube was applied to the eyes to reduce the drying effects of the microscope light during surgery. An SQ or IP injection of Ringer's solution (1 mL/kg) was performed every 1 h to maintain fluid volume, and as necessary to replace lost fluid (for example, due to bleeding). To maintain adequate anesthesia, 1/3 of the initial dose of sodium pentobarbital was given approximately every 45–60 min, and the depth of anesthesia was evaluated every 30–60 min via toe-pinch response and/or an increase of more than 10% in the monitored heart rate. Half of the acepromazine initial dose was injected approximately every 3–4 h. Atropine (the full initial dose) was reinjected after 2–3 h in case of respiratory difficulty.

The gerbils were generally able to self-ventilate, but if an animal appeared to have difficulty breathing, a tracheostomy was performed, and a ventilation tube was inserted into the trachea to ensure breathing without obstruction. Once the gerbil was under deep anesthesia, it was placed on a thermostatically controlled heating pad to maintain a rectal temperature of  $38.5 \pm 1$  °C. The head of the gerbil was firmly fixed using a customized head holder. The pinna and external ear canal of the left ear were removed, and the tympanic bulla on the same side was exposed through a ventral approach in the same surgical field used for the tracheostomy, with care taken throughout to minimize noise and vibration to avoid mechanically induced hearing damage.

The diameter of the opening in the posterolateral wall of the bulla was gradually increased using a small (#15) sharp knife. The tympanic membrane, malleus, incus, stapes, and RWM were all kept intact. SQ electrodes were placed for continuous electrocardiogram (EKG) monitoring. A silver-ball electrode was placed in the round-window niche, and a ground electrode was placed in the soft tissue of the neck or attached to the head holder, to record the compound action potential (CAP). The click sound pressure level (SPL) corresponding to a CAP reading with a peak-to-peak  $|N1-P1|$  amplitude of 15  $\mu$ V was defined as the “threshold” CAP response in this study. The average threshold across four gerbils from

readings taken before and after the *in vivo* 3D-volume measurements were 44.5 and 41 dB SPL, respectively. These values indicate that the general health of the cochlea was maintained throughout the *in vivo* state.

After completing the surgical procedures, the gerbil was carefully transferred to the soundproof chamber to begin OCT imaging. The animal, heating pad, EKG electrode, and surgical bed were transferred to a two-stage goniometer (07-GON-503, Melles Griot, Carlsbad, CA, USA), which was positioned on top of a 3-axis micromanipulator (OCT-XYR1, Thorlabs, Germany). All of these were mounted on a vibration-isolation table. The *in vivo* and PM imaging measurements were performed on the hook region of the cochlea through the intact RWM.

After completing the *in vivo* imaging and physiological measurements, an IP injection of Fatal-Plus (> 150 mg/kg) was administered for euthanasia. The heart typically stops within 5–10 min after injection, at which point the animal stops breathing. The reported PM-state time points are in relation to the moment when the animal stopped breathing, had no heartbeat, and exhibited no other movements.

## OCT System and Volume Scans

All OCT imaging measurements were made using a spectral-domain-OCT (SD-OCT) system with a 905-nm center wavelength, a spectral bandwidth of 213 nm using two light sources, and a 100-kHz high-speed line-scan camera (GAN520C1, Thorlabs, Germany). The system was operated using custom LabVIEW-based software (VibOCT version 1.6). Camera images of the anatomical approach were obtained and used to determine and record the region of interest for the OCT scans (e.g., the black dotted square box in Fig. 1a). VibOCT provides real-time depth-resolved 1D A-scan, 2D cross-sectional B-scan, and 3D volumetric C-scan imaging. The axial resolution was  $\sim 1.4 \mu\text{m}$  (in water, with a refractive index of 1.33), and the lateral resolution was  $\sim 1.95 \mu\text{m}$ , using a 30.5-mm, 0.26-NA long-working-distance,  $10\times$  objective lens (M Plan Apo NIR, Mitutoyo, Aurora, IL, USA). To minimize variations among the 3D-volume OCT scans across animals, the orientation of the gerbil head in the head holder, as well as settings on the positioning stage and goniometer, were kept similar across experiments.

While the penetration depth of the OCT system is approximately 1.44 mm (in water), the best B-scan image quality was obtained for a depth range of less than 300  $\mu\text{m}$ , which also avoided mirroring effects. Because the effective depth of field is smaller than the depth range of interest of about 1–1.2 mm, three or more 3D volume scans were acquired at different focal depths and tracked by the fine-focus adjustment on the OCT optical head with  $\sim 1\text{-}\mu\text{m}$  resolution using a Vernier scale. A single 3D volumetric C-scan consists of a longitudinal stack of 512

B-scans that are each composed of 512 A-lines across, and each A-line is in turn composed of 1024 depths. Each B-scan volume is averaged 10 times.

All sub-volume scans (each covering a different depth range) were independently processed using ImageJ software (ImageJ.nih.gov) and concatenated to obtain a complete volume stack as follows: (1) the sub-volume scan was resliced from the measured sagittal plane (cross-sectional view) to the desired transverse plane (top-to-bottom view), (2) the region of interest was cropped, typically to 300  $\mu\text{m}$ , and (3) the non-overlapping portions from each depth range were aligned, and those portions were then concatenated to obtain a full volume of the OoC at the basal end of the cochlea (i.e., the hook region), including the RWM and Reissner's membrane.

All OoC-structure and fluid-space volumes were segmented from the 3D-volume OCT measurements. More details on the 3D-reconstruction and segmentation methods for the OoC structures and the fluid spaces of the OoC and ST are provided in the following section.

## Segmentation Methods

The software applications Amira (version 2019.1; Thermo Fisher Scientific; Waltham, MA, USA) and SimpleWare ScanIP (version P-2019.09; Synopsis; Exeter, UK) were used to acquire 3D reconstructions and segmentations of the cochlear structures, respectively. The images in the OCT volume stacks were segmented semi-automatically using a combination of thresholding, morphological operations (e.g., dilation, erosion, etc.), as well as smoothing and interpolation tools, then reconstructed into 3D objects in both SimpleWare and Amira. The segmented objects were then analyzed to extract the total width and height of the OoC ( $\text{OoC}_W$  and  $\text{OoC}_H$ , respectively), the respective widths of the arcuate ( $\text{AZ}_W$ ), and pectinate ( $\text{PZ}_W$ ) zones of the BM, and the OoC area (Fig. 2a).

Figure 2b shows a reconstructed 3D representation of a portion of the hook region that extends about 1.1 mm from the basal end of the cochlea (white dotted arrow), assembled from stacks of  $1024 \times 512$  2D OCT cross-sections, such as the one shown in Fig. 2a. The OoC structure is shown as the orange region between the osseous spiral lamina (OSL) and spiral ligament (SL) ridge.

Figure 2c shows a top-down view of the segmented OoC structure, with the RWM and secondary spiral lamina (SSL) hidden, and a white dividing line added between the arcuate-zone ( $\text{BM}_{AZ}$ ) and pectinate-zone ( $\text{BM}_{PZ}$ ) regions of the BM. The boundary between the  $\text{BM}_{AZ}$  and  $\text{BM}_{PZ}$  regions coincides with the location of the junction of the outer pillar cell (OPC) and the base of the first row of Deiters' cells (DCs).  $\text{OoC}_W$  is the sum of  $\text{AZ}_W$  and  $\text{PZ}_W$  (Fig. 2a).

Centerlines were determined for the fluid-space volumes, such that circumscribed ellipses orthogonal to the centerline were fit to the shape of each cross section along

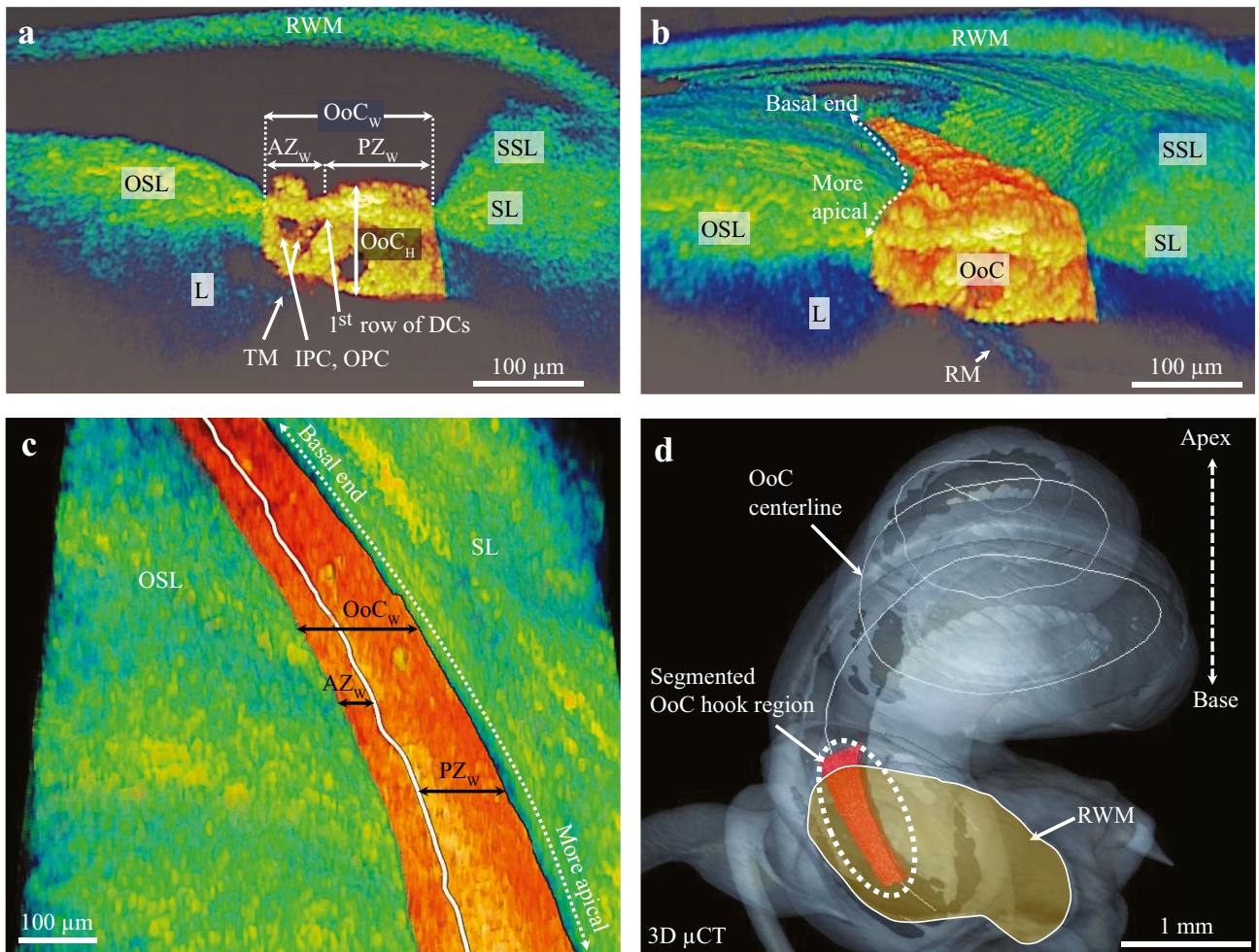


**FIG. 2.** Segmenting the organ of Corti (OoC) in the hook region and determining  $OoC_w$ ,  $AZ_w$ , and  $PZ_w$ . **a** An *in vivo* 2D OCT cross-sectional image (from animal #191) shows the OoC structure (orange color), with the defined widths ( $OoC_w$ ,  $AZ_w$ , and  $PZ_w$ ) and height ( $OoC_H$ ) labeled, as well as other structures whose abbreviations are defined in the caption to Fig. 1. Note that the actual widths and heights were calculated with respect to curved longitudinal centerlines rather than the imaging plane as depicted here (see Fig. 3). **b** A 3D reconstruction from the same ear, based on

*in vivo* OCT volume scans, indicates the segmented OoC structure in the hook region (orange color) between the OSL and SL ridge, from the basal end toward a more-apical position (white dotted line). **c** A view of the segmented OoC structure with a white line dividing the  $AZ_w$  and  $PZ_w$  subdivisions of the BM ( $OoC_w$ ), and with the RWM and SSL removed for better visualization of the segmented OoC structure. **d** The OCT-based segmented region of the OoC (red) is shown superimposed upon the hook region of a  $\mu$ CT-based whole-cochlea reconstruction from a different ear (gray).

the length of the volume. The major and minor axes of these ellipses were then used to gauge the varying cross-sectional shapes of each fluid space. The centerlines were calculated in SimpleWare based on the Skeletonization algorithm.

The ISS volume is mostly bounded by the tectorial membrane (TM), limbus (L), and inner-sulcus cells (ISCs; Fig. 1d). The ISS-TM boundary was not always visible in all scans. When this boundary was not visible, it was approximated by projecting a line between the edge of the L and inner hair cell (IHC; Fig. 1b, d). A portion of the OT boundary is formed by tectal cells (TCs; Fig. 1d), which can be mistaken as Hensen's cells (HCs; Fig. 1d) (Henson et al. 1983). Tectal cells are morphologically

distinct from Hensen's cells, because their membranes form part of the OT fluid space and they are not in contact with the BM (Spicer and Schulte 1994). The outer wall of the OT is made up of tectal cells, by the tectal-cell extension (TCE), and the medial boundary is formed by the third row of phalangeal processes (PhPs), OHCs, and DCs (Fig. 1d).

### Comparisons to a $\mu$ CT-Based Whole-Cochlea Reconstruction

A gerbil temporal bone previously scanned (Jackson 2014) using X-ray-based  $\mu$ CT imaging (vivaCT 40  $\mu$ CT scanner, SCANCO Medical AG; [www.scanco.ch](http://www.scanco.ch)) was

used to estimate the starting position for each individual OCT scan. The  $\mu$ CT scan was obtained using an energy of 55 kV (peak), a current dose of 145  $\mu$ A, a 0.5-mm aluminum filter, 1000 projections/180° with 2048 total projections, and a voxel size of 12.5  $\mu$ m. The 3D volume of the cochlea was obtained by segmenting the image stack and thresholding. The bony primary and secondary OSL edges were used to approximate the BM width and determine the OoC centerline from base to apex, using Amira. This  $\mu$ CT-based BM centerline of a whole-cochlea reconstruction was then used to register each segmented OCT-based volume at its most likely location in the hook region by visually aligning in 3D using the round-window opening as a landmark and the curvature of the OoC structure for guidance. Figure 2d shows an example of an OCT-based segmented OoC-structure volume (the red region within the white dotted ellipse) whose centerline has been registered with the  $\mu$ CT-based whole-cochlea OoC centerline. By aligning the centerlines, the estimated starting points of the OCT-based

volumes ranged from 78 to 228  $\mu$ m from the basal end of the cochlea, with each volume extending approximately 1.1 mm in the apical direction.

### Determining $OoC_W$ and $OoC_H$ from OCT Data

The  $OoC_W$  measurements were conducted with respect to planes orthogonal to the BM centerline.

Figure 3a contains a 2D cross-sectional OCT image showcasing the thin BM layer (red region with white dotted outline) segmented using the volume-editing tool in Amira. Figure 3b shows a 3D view of the thin BM layer (in red), from the basal end to a more-apical location, with the rest of the segmented OoC structure shown in gray.

The total width of the OoC ( $OoC_W$ ) was determined by fitting circumscribed circles around the BM layer, as illustrated in Fig. 3c for a 2D cross section. Rather than determining the width based on a projection onto the imaging plane, however, the segmented BM was instead

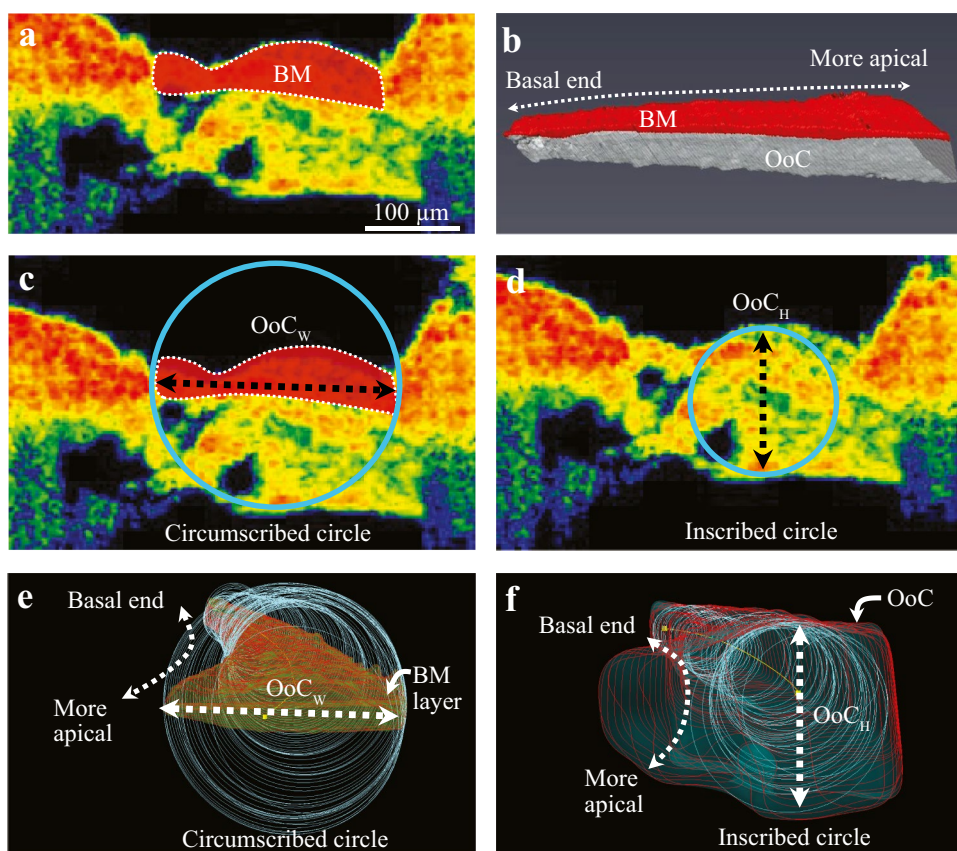


**FIG. 3.** Determining the width and height of the OoC along the cochlear length by fitting circles along the centerline in 3D. **a** A 2D OCT cross-sectional image of the OoC with the BM layer inside the white-dotted outline (from animal #269). **b** The segmented 3D volume of the OoC structure (gray) is shown with the segmented BM volume layer (red) on top. **c** An illustration showing how a circumscribed circle around the thin BM layer can be used to determine the width of the OoC ( $OoC_W$ ). **d** An illustration showing how an

inscribed circle can be used to determine the height of the OoC ( $OoC_H$ ). **e** To determine  $OoC_W$ , the segmented structure of the thin BM layer was fitted with circumscribed circles perpendicular to the centerline (light blue; spaced 8- $\mu$ m apart along the centerline). **f** To determine  $OoC_H$ , the full segmented OoC volume with the BM layer on top was fitted with inscribed circles perpendicular to the centerline (light blue; spaced 8- $\mu$ m apart along the centerline).

imported into SimpleWare to calculate the centerline and fit each circumscribed circle so that it is perpendicular to the centerline (Fig. 3e). The diameter of each of these circles, spaced at 5-voxel (8- $\mu\text{m}$ ) intervals, corresponds to  $\text{OoC}_W$  at each longitudinal location.  $\text{OoC}_W$  is equivalent to the sum of  $\text{AZ}_W$  and  $\text{PZ}_W$  (Fig. 2c).

The height of the OoC ( $\text{OoC}_H$ ) was determined using a similar inscribed-circle fitting procedure for the total OoC volume, as illustrated in Fig. 3d for a 2D cross section. As for the width, the segmented OoC structure was imported into SimpleWare to calculate the centerline and fit inscribed circles perpendicular to the centerline. The diameters of these inscribed circles, also spaced at 5-voxel (8- $\mu\text{m}$ ) intervals (Fig. 3f) represent  $\text{OoC}_H$  at each longitudinal location.

### Histological Preparations and Reconstructing 3D Image Stacks

The anatomies of four ears from two gerbils (#274 and #338, both ears) were quantified using histological methods. Animal #338 was not subject to any OCT measurements before histological processing, but in vivo OCT measurements were performed on the left ear of animal #274 beforehand. The processing steps consisted of tissue fixation (using a 4% formaldehyde, 1% acetic acid, 0.1% glutaraldehyde solution) followed by celloidin embedding (O'Malley et al. 2009). Each animal was first intracardially perfused, and then its whole head was extracted, decalcified, and H&E stained, all of which was performed by the Otopathology Laboratory at MEE. Serial sections of the whole skull, including both individual ears, were cut (along the sagittal plane) into 20- $\mu\text{m}$ -thick slices, with every other slice stained to create histology slides. Thus, the histology sections were spaced at 40- $\mu\text{m}$  intervals. The slides were digitized and then reconstructed and segmented into 3D volume stacks for direct comparison against the OoC morphology as obtained using OCT methods.

The histology slides from the gerbil cochleae were digitized using a Nikon® E800 microscope equipped with a Nikon® DS-Ri2 digital camera. The whole cochlea was imaged with  $5\times$  magnification, and with  $20\times$  magnification for higher-resolution measurements of the OoC hook region. The digitized histology sections were then aligned and segmented using Amira.

The OoC centerline from each reconstructed histology volume was aligned to that of the  $\mu\text{CT}$ -based whole-cochlea reconstruction (as described above) to estimate the starting location of the histology volume near the basal end of the cochlea. Based on this alignment, the distance from the basal end of the cochlea to the same starting location used for the OCT imaging was defined along the OoC centerline. The 3D reconstructions of the OoC fluid spaces from OCT and histology were aligned, analyzed, and compared in Amira.

## RESULTS

We used 3 female and 2 male gerbils for the in vivo studies ( $N=5$ ), with a subset of these ( $N=3$ ; 2 male, 1 female) also used for the PM studies. For each gerbil, in vivo 2D cross-sectional images (e.g., Fig. 1b) were acquired at  $\sim 5$ -min intervals over a 60-min period before the time of death. For three of the gerbils, 2D cross-sectional images continued to be acquired over a 90-min PM period. Using a consistent angular approach, 3D-volume scans (e.g., Fig. 1c; Movie SI-1) were acquired in vivo at the beginning of the experiment and 60 min later, just before death, and at 10-, 30-, 60-, and 90-min after death.

Figure 4 shows representative 2D images at selected time points of the living (top row), and PM (rows 2 and 3) cochlear states. The in vivo OoC structures and fluid spaces remained stable across the 60-min interval. In the living cochlea, the RWM and Reissner's membrane were curved and bulged outward away from the OoC. A time-lapse movie from the same ear (Movie SI-2) shows significant changes occurring in the cochlear anatomy after death. The middle row of Fig. 4 shows that both the RWM and Reissner's membrane have started to recede toward the OoC as early as 10-min PM. By 60-min PM, the RWM and Reissner's membrane have changed their directions of curvature, indicating decreased volumes of the ST and scala media. This is consistent with PM decreases in both the ST pressure and the pressure difference between the scala media and scala vestibuli. The dimensions of rigid structures such as the OPC that separate the ToC from the SN (Fig. 1d) generally appear stable throughout.

### Quantitative Assessment of OoC Structural Changes from In Vivo to Postmortem

Figure 5a shows a 2D cross-sectional OCT image illustrating the gross dimensions of the OoC important for cochlear mechanics. The dimensions and volume of the OoC structure were measured for the in vivo and PM states and then compared.

In the image,  $\text{OoC}_W$  is bounded by the OSL to the left and the SL to the right.  $\text{OoC}_H$  is bounded by the BM at the top and a combination of the reticular lamina (RL), TCs, and HCs at the bottom. The volume of the OoC cellular elements was calculated by subtracting the area of the fluid spaces (see Fig. 7) and integrating the remaining area along the longitudinal dimension. In the region evaluated, the volume per unit length of the OoC structural components increased on average by about 25% by 90-min PM (Fig. 5b). This increase in volume is likely due to swelling of the OoC cells.

The width ( $\text{AZ}_W$ ) and collagen-fiber content of the arcuate zone of the BM ( $\text{BM}_{AZ}$ ) are thought to play a

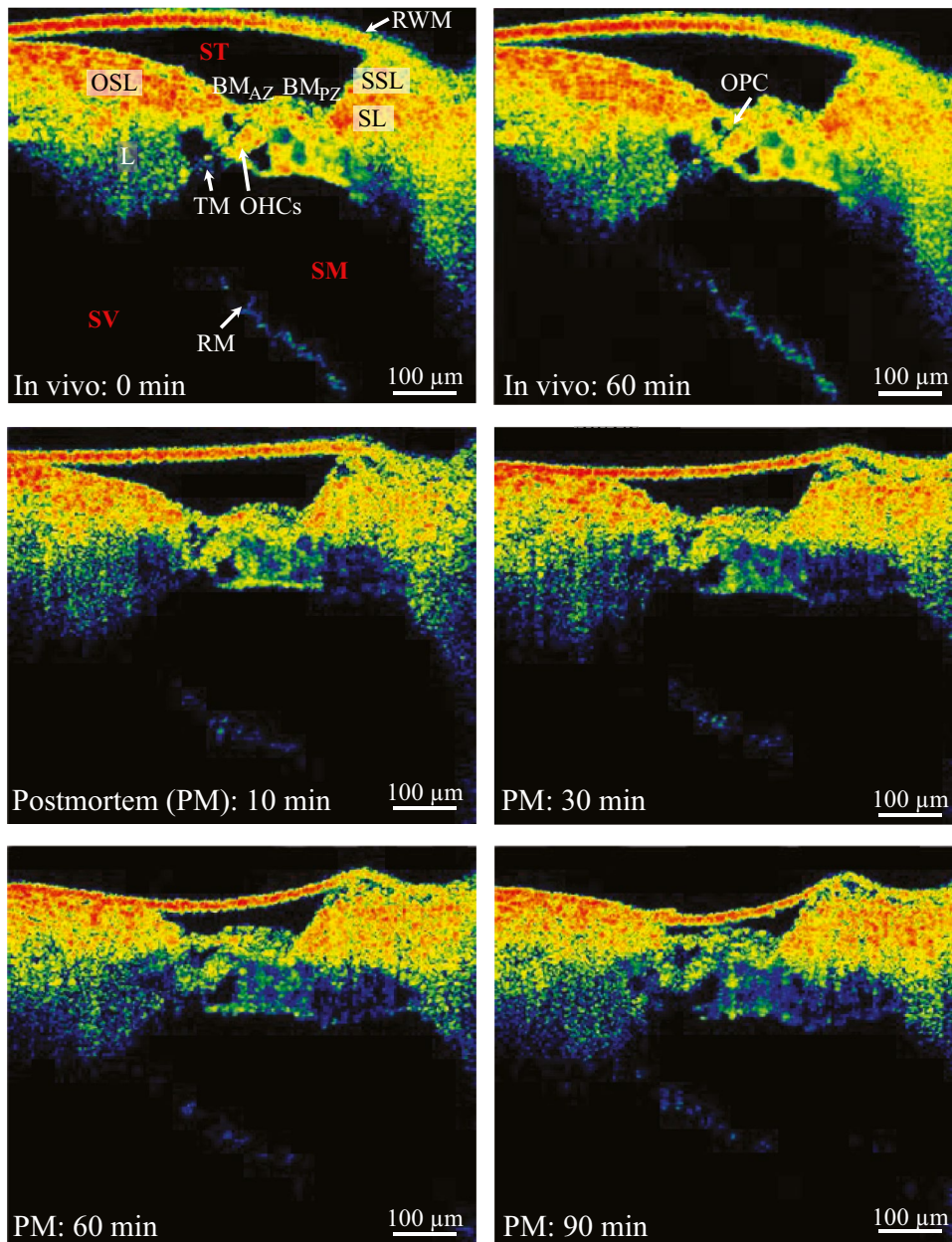


**FIG. 4.** OCT-based cross-sectional OoC images (from animal #269) at two in vivo times 60-min apart (top row) and four postmortem (PM) times, at 10, 30, 60, and 90 min after death (rows 2 and 3). The similarities between the in vivo images indicate the stability of the living preparation. The sequence of PM images reveals the

progression of changes to the cochlear morphology after death. The full set of cross-sectional images of the PM state, acquired at 5-min increments, can be viewed as a time-lapse sequence (Movie [SI-2](#)). See the caption of Fig. 1 for a list of abbreviations.

dominant role in the place–frequency tonotopic map of the gerbil cochlea (Kapuria et al. 2017). The total width of the BM ( $OoC_W$ ) has been divided into  $AZ_W$ , bounded by the OSL and the junction of the outer pillar cell and base of the first-row DCs, and  $PZ_W$ , the width of the pectinate zone of the BM ( $BM_{PZ}$ ), which is bounded by the base of the first-row DCs and the SL, as defined previously (Plassmann et al. 1987; Richter et al. 2000).  $OoC_W$  is equivalent to the sum of  $AZ_W$  and  $PZ_W$ .

Figure 5c–f contains plots of  $AZ_W$ ,  $PZ_W$ ,  $OoC_W$ , and  $OoC_H$  as functions of distance from the basal end of the cochlea toward the apex in the hook region over the  $\sim 0.1$ – $1.1$ -mm range. The starting position relative to the basal end of the cochlea was slightly different for each OCT scan. The individual in vivo results are shown (thin colored lines;  $N=5$ ), along with their mean  $\pm$  SD (thick blue lines and error bars), as well as the mean  $\pm$  SD ( $N=3$ ) for the 90-min-PM case (thick



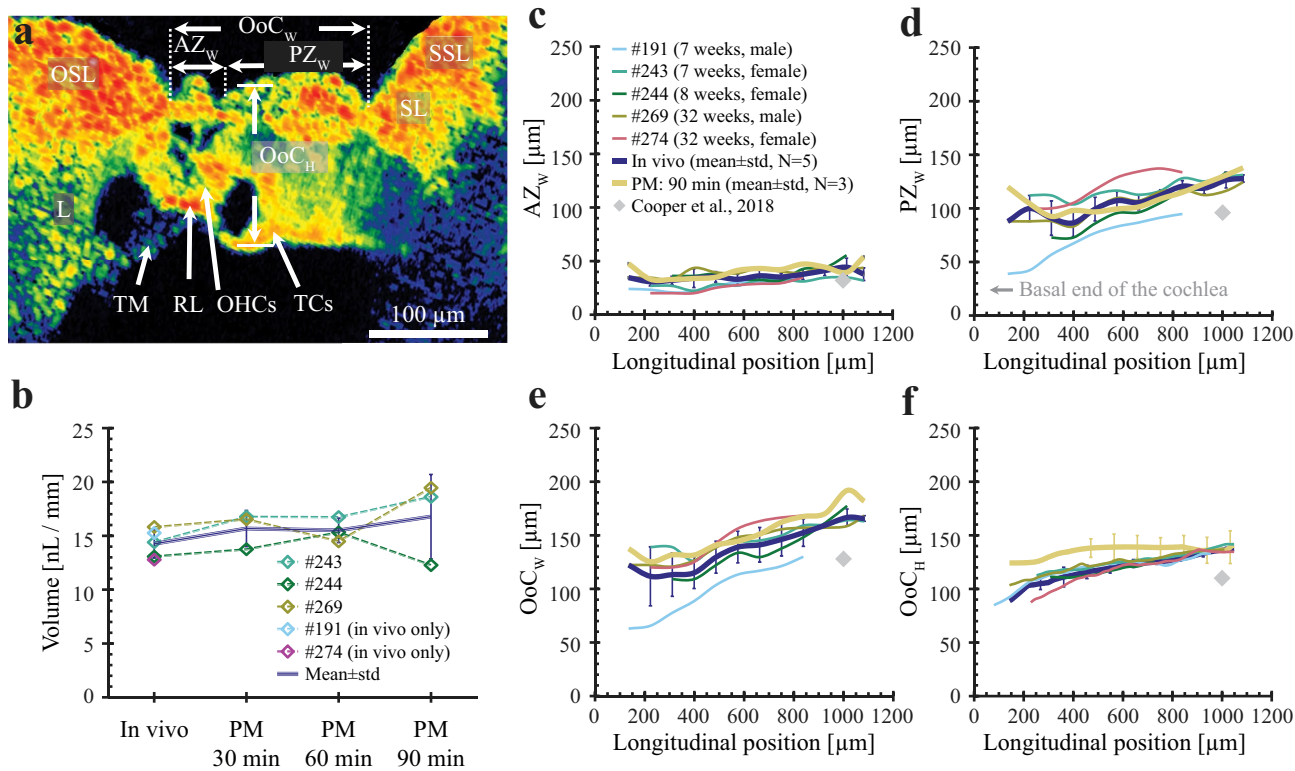


**Fig. 5.** OoC volume across in vivo and PM animal states, and OoC linear dimensions as functions of longitudinal position in the cochlear hook region. **a** This 2D cross-sectional image (from animal #243) identifies the  $BM_{AZ}$  width ( $AZ_w$ ) between the OSL ridge and the base of the first row of DCs, the  $BM_{PZ}$  width ( $PZ_w$ ) between the base of the first row of DCs and the SL ridge, and the total OoC width ( $OoC_w$ ) between the OSL and SL ridges, which is equivalent to the sum of  $AZ_w$  and  $PZ_w$  (see fitted circumscribed circle in Fig. 3c). The overall OoC height ( $OoC_h$ ) is defined as the distance between the BM and the TCs or TCE (see fitted inscribed circle in Fig. 3d). **b** Changes in the OoC volume (without the OoC fluid spaces) per unit length (nL/mm) over time, from in vivo ( $N=5$ ) to

90-min PM ( $N=3$ ), along with the mean and standard deviation (SD). **c–f** The  $AZ_w$ ,  $PZ_w$ ,  $OoC_w$ , and  $OoC_h$  dimensions are plotted in respective panels as functions of longitudinal position (in  $\mu\text{m}$ ) from the basal end of the cochlea. The mean  $\pm$ SD error bars for the in vivo measurements ( $N=5$ ) are shown as thick blue lines, and those for the 90-min-PM measurements ( $N=3$ ) are shown as thick yellow lines. Individual in vivo cases (thin colored lines) are also shown, with the ID, age, and gender of each animal reported in panel c. In **c–f**, the gray diamonds are comparison measurements from in vivo OCT images reported by Cooper et al. (2018) for a location about 1 mm ( $\sim 40$  kHz region) from the basal end of the gerbil cochlea.

yellow lines and error bars). While  $OoC_w$  and  $OoC_h$  are slightly larger for the PM state than for the in vivo state, the error bars indicate that they are not expected to be significantly different and thus we did not perform statistical analyses on any of the width or height measurements.

Generally, the dimensions of the OoC increase from the base toward the apex (Fig. 5c–f), which is consistent with the decreasing characteristic frequency in the apical direction that is a key feature of the mammalian cochlea (Peterson and Bogert 1950; Von Békésy 1960). Despite the increases in all these dimensions as one moves apically, the  $AZ_w/OoC_w$  ratio maintains an approximately constant value of around 0.25 (not shown). As a comparison, we estimated the OoC dimensions based on an in vivo OCT image near the 1-mm location, from Fig. 1c of (Cooper et al. 2018). These dimensions (gray diamonds in Fig. 5c–f) are typically lower than the averages we found, by about 25%. Our measurements in

animal #191, which was the youngest and one of the lower-weight animals studied (7 weeks, 72 g), are also lower than our average. The Cooper et al. animal was about 12 weeks and 56 g. Thus, the differences between our overall results and those of Cooper et al. could be due to lower animal weights, and/or perhaps different OCT-beam angles. Similar age and weight-related differences in OoC dimensions have been documented in human infants vs. adults (Meenderink et al. 2019).

### OoC Fluid-Space Dimensions from In Vivo to 90-min Postmortem

Figure 6 reports the major and minor axes of the OoC fluid subspaces as functions of cochlear location. These subspaces were roughly elliptical in cross-section (Fig. 6a). Segmentations of the ISS, ToC, SN, and OT fluid spaces for a representative ear are presented in Fig. 6b–e. Panels

b-i-e-ii of Fig. 6 show the individual in vivo results (thin colored lines), the corresponding mean  $\pm$  SD ( $N=5$ , thick blue lines and error bars), and the mean  $\pm$  SD for the 90-min-PM results ( $N=3$ , thick yellow lines and error bars), for the lengths of the major (b-i-e-i) and minor (b-ii-e-ii) axes. Additionally, the minor/major axis-length ratios are shown for the in vivo (blue lines) and 90-min-PM (yellow lines) means (b-iii-e-iii).

The ISS fluid space had the largest in vivo dimensions of the OoC fluid spaces. The average length of the ISS major axis for the in vivo case (Fig. 6b-i) generally increased with longitudinal position, reaching a maximum of about 68  $\mu\text{m}$  near the 1000- $\mu\text{m}$  mark. At 90-min PM, the average length of the ISS major axis was smaller. Unlike the major axis, the ISS minor axis for the in vivo case (Fig. 6b-ii) exhibited a flatter longitudinal profile on average, with a value of about 40  $\mu\text{m}$  in the

200–1000- $\mu\text{m}$  range. At 90-min PM, the average length of the ISS minor axis was smaller. In general, the ISS major axis (Fig. 6b-i) showed a similar longitudinal profile between the in vivo and 90-min-PM cases, but with the in vivo case scaled higher.

Other OoC dimensions shown in Fig. 6 include the ToC (c-i-c-iii), SN (d-i-d-iii), and OT (e-i-e-iii). For the ToC and SN, the PM changes relative to in vivo were minimal. The 90-min-PM OT dimensions (Fig. 6e-i-ii) generally increased relative to the in vivo case for longitudinal positions apical to the 500- $\mu\text{m}$  location.

The minor/major axis-length ratios indicate the degree to which the cross section of the fluid space is circular (0.75–1.0), elliptical (0.5–0.75), or oblong (<0.5; Fig. 6, bottom row). In general, the ISS (Fig. 6b-iii) was elliptical in cross section and did not change much from in vivo to 90-min PM. The ToC (Fig. 6c-iii) and OT (Fig. 6e-iii)

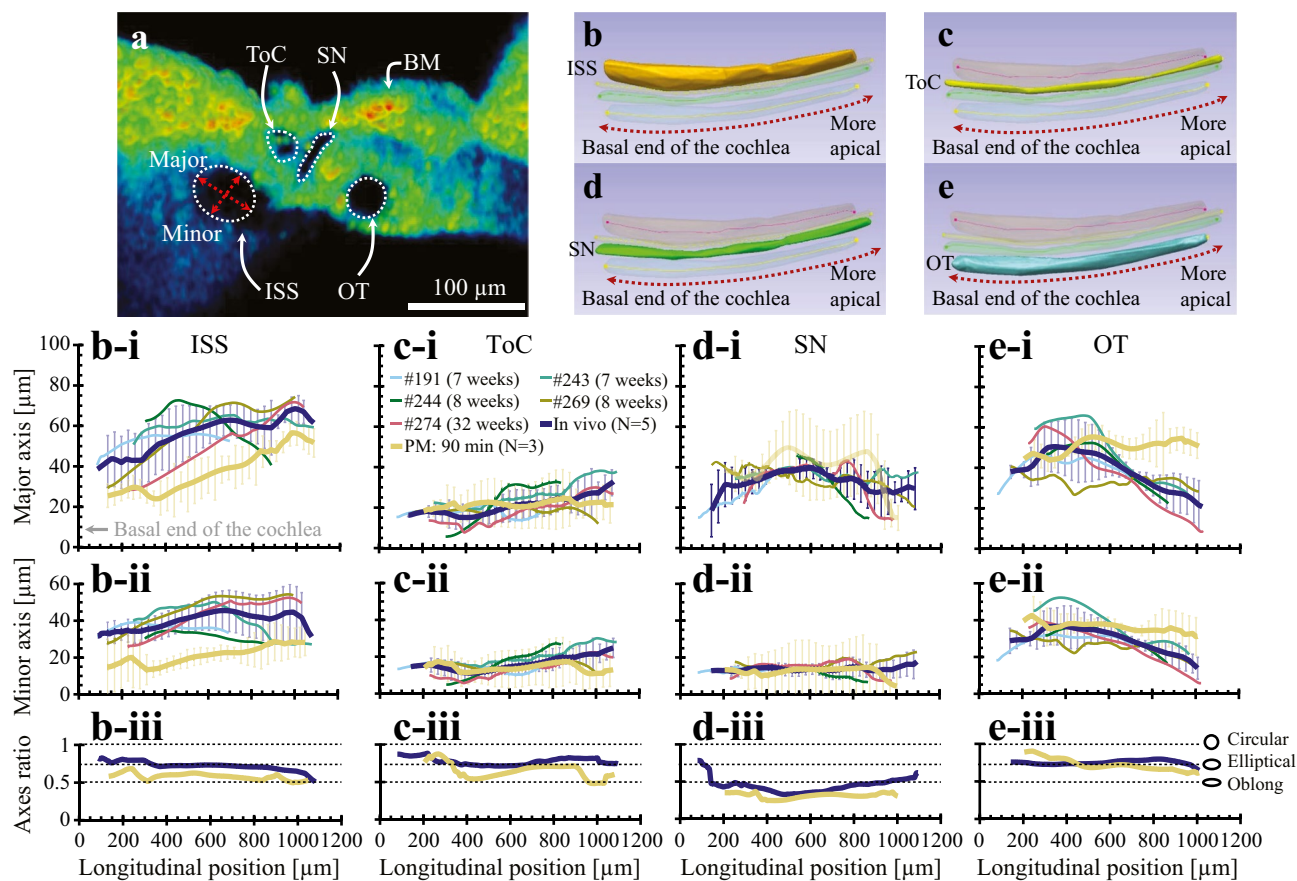


**FIG. 6.** **a** A 2D OCT cross-sectional image with the BM, ISS, ToC, SN, and OT labeled (from animal #191). Representative in vivo volume segmentations are shown of **b** the ISS, **c** the ToC, **d** the SN, and **e** the OT, for an approximately 1-mm-long basal section of the cochlea. The inside dimensions of each tubular shape were defined by the major and minor axes of their elliptical cross sections (e.g., red crossed arrows in **a**). Each ellipse was placed orthogonal to the centerline that best fit the space at each position. **b-i** to **e-iii** Inner dimensions of the OoC fluid spaces and minor/major axis-length

ratios, for in vivo and 90-min-PM animal states, as functions of longitudinal position in the cochlear hook region. The mean  $\pm$  SD results are in thick blue lines for the in vivo cases ( $N=5$ ) and in thick yellow lines for the 90-min-PM case ( $N=3$ ). Individual in vivo results are shown as thin colored solid lines, with the ID and age of each animal reported in the legend of panel **c-i**. The second row (**b-i** to **e-i**) shows the corresponding major-axis lengths, while the third row (**b-ii** to **e-ii**) shows the minor-axis lengths. The last row (**b-iii** to **e-iii**) contains the minor/major axis-length ratios.

were generally circular for the in vivo case and changed somewhat at 90-min PM. The SN (Fig. 6d-iii) was generally more oblong than the other fluid spaces.

To better quantify the progression of PM changes over time, Fig. 7 plots the OoC fluid-space volumes for the in vivo state and three PM states 30 min apart. Figure 7 a, b shows segmented 3D OCT volume images for a representative animal (#269) for the in vivo (Fig. 7a) and 90-min-PM (Fig. 7b) states. The decrease in ST volume (purple) after death is readily apparent. Figure 7 c–g contain plots of the ST, ISS, ToC, SN, and OT volumes (normalized by the longitudinal length of the segmented region) as time progresses, for three animals. The volumes of both the ST (Fig. 7c) and ISS (Fig. 7d) decreased systematically from in vivo to 60-min PM. The ISS volume recovered slightly by 90-min PM, whereas the ST volume continued to decrease. The ToC and SN volumes did not change (Fig. 7e, f). On the other hand, the OT volume (Fig. 7g) increased slightly from in vivo to 90-min PM.

### Statistical Analysis

Our hypothesis is that the measured volume of each anatomical feature is a function of animal state (Figs. 5b and 7). To determine the significance of the volume trends reported in Fig. 7, we performed an analysis of variance

(ANOVA) with two independent categorical variables using the built-in MATLAB function `anova2` (MATLAB R2020a; Natick, MA, USA). The first variable was the animal state, consisting of in vivo, 30-min-PM, 60-min-PM, or 90-min-PM categories. The second variable was the anatomical feature of interest, with categories consisting of the ST, OoC structure, and each of four OoC fluid subspaces. The `anova2` analysis indicates that the different animal-state categories were statistically independent  $p < 1E-5$ . The different anatomical-feature categories were also deemed statistically independent, with  $p < 1E-5$ , as was the interaction between the animal-state and anatomical-feature variables, with  $p < 1E-5$ . The statistical independence among animal-state categories indicates that the measured volumes for the in vivo state and each of the three PM states are different, which addresses one of the questions posed by this study. With statistical independence of all measured volumes in the different categories established, we then went on to determine the PM changes of individual anatomical volumes by performing a one-way ANOVA analysis for each, with the animal state as the independent variable.

Of the six anatomical volumes measured (Figs. 5b and 7), there were no significant changes across the four animal states for the OoC structure, SN, and ITC. The other three fluid-space volumes, for the ST, ISS, and

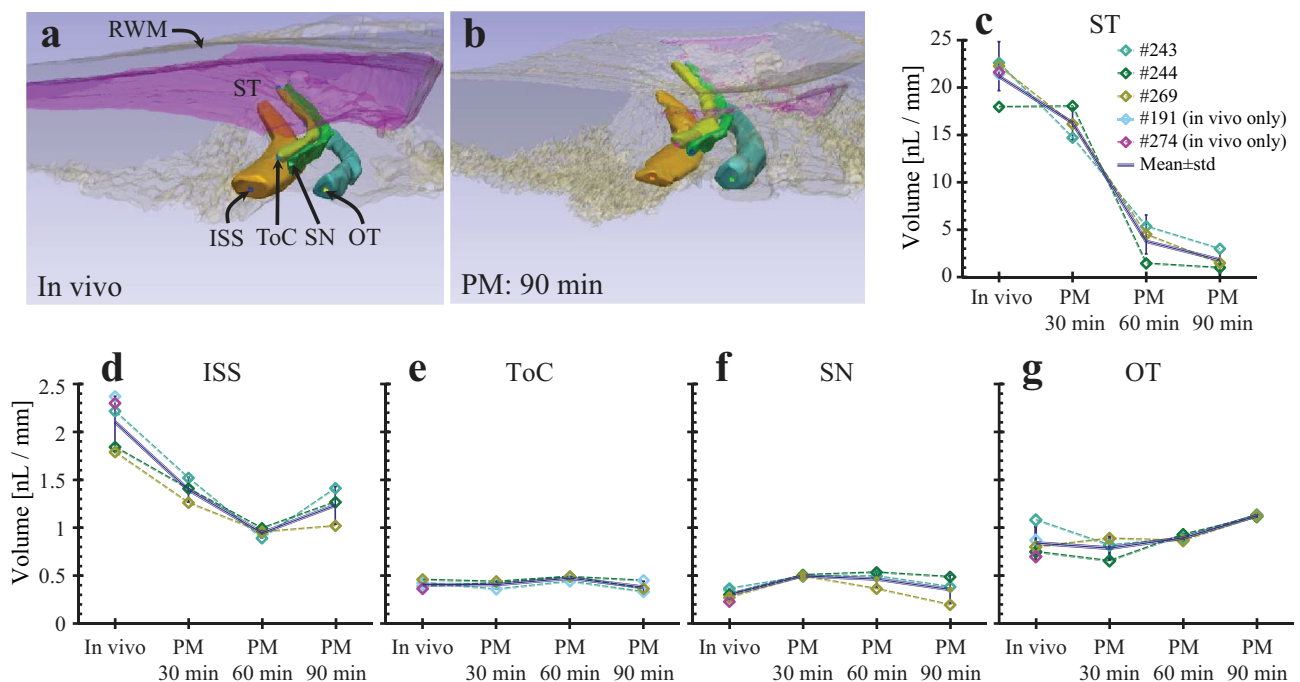


**FIG. 7.** Death-related changes to the ST and OoC fluid volumes. **a–b** 3D reconstructions of the ST and OoC fluid spaces (ISS, ToC, SN, and OT) based on OCT scans of a representative ear (#269), taken in vivo **a**, and 90 min after death **b**. **c–g** The volume per unit length (nL/mm) is plotted for the in vivo and PM animal states, for

the ST **c**, ISS (**d**; note the change in scale for the bottom row), ToC **e**, SN **f**, and OT **g**. The mean  $\pm$  SD error bars are shown as solid blue lines, and the results from individual ears are shown as colored dashed lines. Note that each volume is from an approximately 1-mm-long longitudinal section.

OT, did change significantly with animal state. Pairwise comparisons among the four animal states results in six possible combinations of  $p$ -values, and these are shown in Fig. 8 for each of these three volumes. For significance, we use the  $p_0=0.05$  criterion. There were significant ( $***p<0.0002$ ) decreases in the ST volume by more than a factor of 10 from in vivo to 60-min and 90-min PM (Fig. 8a), but not from in vivo to 30-min PM. Thus, it took more than 30 min to elapse after death for significant volume changes to take place in the ST. Of the OoC fluid spaces measured, the ISS volume changed the most after death (Fig. 8b). From in vivo, there was a decrease in ISS volume by about 35% at 30-min PM ( $*p<0.02$ ), and it decreased further by about 55% at 60-min PM ( $***p<0.002$ ). The increase in OT volume by 40% from 30-min PM to 90-min PM ( $*p<0.02$ ) may be related to the increase in the OoC-structure volume (although this change was not significant). If we further apply a Bonferroni correction (dividing our  $p_0$  by the 6 possible combinations, such that our criterion for significance is reduced to  $p_0=0.0083$ ), then the  $**$  and  $***$  values remain significant. This means that by 60-min PM the ST and ISS volumes changed by a significant amount.

### OCT vs. Histology Comparisons

In histological preparations of the cochlea, distortions of the cochlear tissue can arise in multiple ways. In Figs. 5, 6, 7, and 8, we demonstrate and quantify the distortions to the in vivo OoC morphology that took place due to death alone, particularly for the ST and ISS. Additional well-known factors that can distort the OoC structure and fluid spaces include tissue fixation, decalcification, dehydration, embedding, and staining procedures required for histological tissue preparation (Merchant and Nadol 2010). To quantitatively assess the degree of combined

OoC distortions due to death and histological processing, the OoC morphology was measured after processing with histological methods ( $N=4$ ).

Figure 9a shows the hook region in the gerbil cochlea (#274) obtained through histological methods at approximately the same location as the OCT cross-sectional image at  $\sim 560\ \mu\text{m}$  from the basal end of the cochlea (Fig. 1b). In Fig. 9a, the TM appears detached, which is sometimes the case with histology, whereas it appears to be normally attached (but less visible) in the in vivo OCT image (i.e., Figs. 1b and 5a). In the histological preparation, not only are the SN and ToC fluid spaces hard to distinguish from the OoC structures, but also the OT fluid space is dramatically reduced (white dotted circle in Fig. 9a), and the dimensions of the OoC structures appear significantly smaller than those of the in vivo OCT image, especially the OoC<sub>H</sub> dimension.

The OoC dimensions measured with OCT can be compared against those measured by histology. Figure 9b shows the mean  $\pm$  SD volume/mm of the ST in animals processed with histology (based on four ears from two animals; green diamond with error bars), and from an individual ear measured using both in vivo OCT and histology (#274; magenta triangle and diamond, respectively). The histology-based ST volume for the individual animal (magenta diamond) was about 50% greater than the mean histology-based volume across ears (green diamond). However, the in vivo OCT-based volume on the same individual ear (magenta triangle) was about three times greater than the histology-based volume. The histology-based volume was comparable to the average of the 60- and 90-min PM volumes. Figure 9b shows that a significant amount of the change in ST volume took place between 30- and 90-min PM. For histological processing, the animal was perfused in vivo with a fixative that takes effect within 5 min. In the absence of this perfusion step,

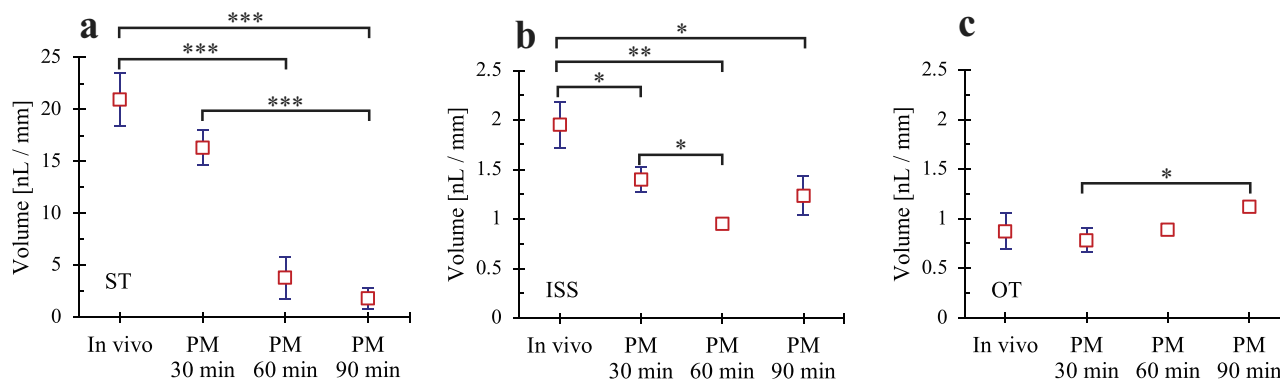


**FIG. 8.** The mean  $\pm$  SD ( $N=3$  animals, for which all measurements were available) of the volumes per unit length (nL/mm) of the **a** ST, **b** ISS, and **c** OT, for each animal state (note the change in scale for **b** and **c**). The  $p$ -values between pairs of animal states, from an ANOVA test, are indicated by horizontal brackets between the

states being compared. The number of asterisks above each bracket correspond to the following degrees of statistical significance:  $*p<0.02$ ,  $**p<0.002$ , and  $***p<0.0002$ , all of which are of greater significance than the  $p_0=0.05$  criterion. Some error bars are too small and are concealed by the symbol representing the mean.

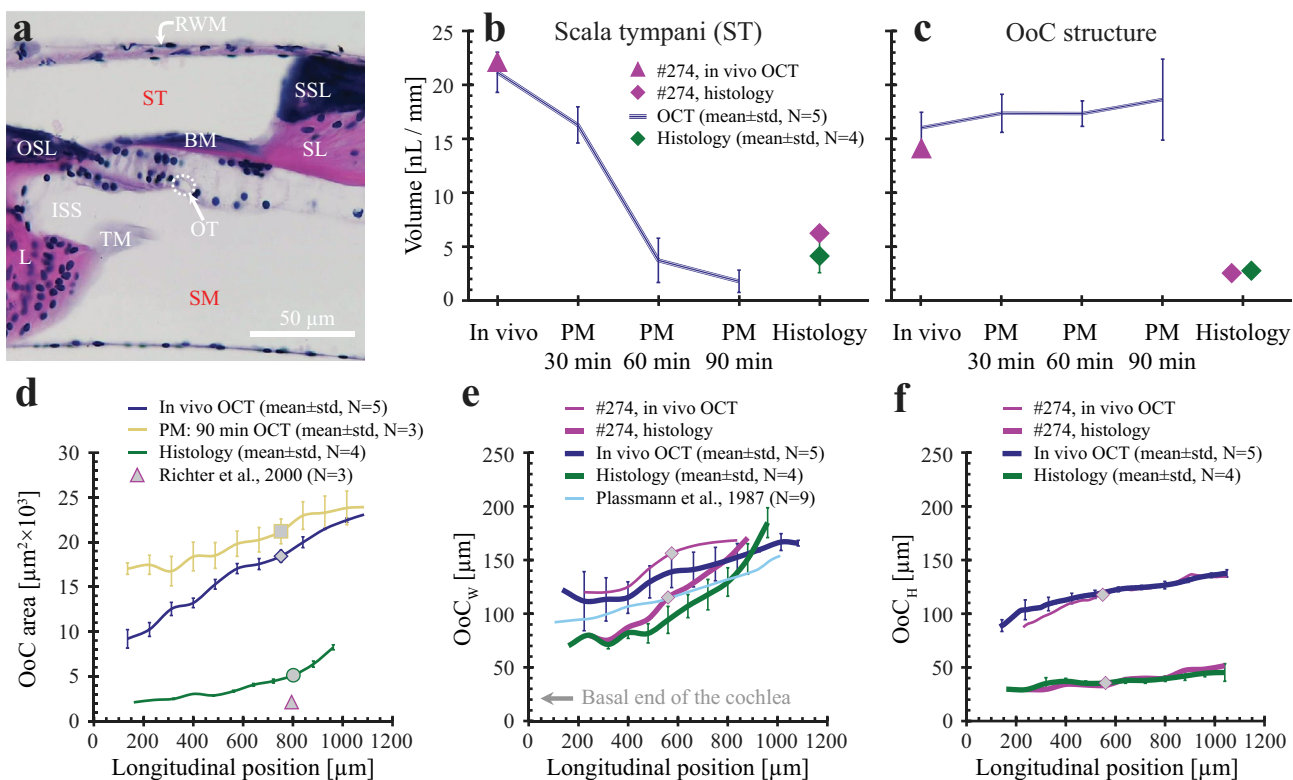


**Fig. 9.** Comparisons of cochlear measurements between OCT (in vivo and PM) and histology (PM only). **a** An image of a histological OoC cross section (from the left ear of animal #274) at a location  $\sim 560 \mu\text{m}$  from the basal end of the cochlea. **b–c** The volumes per unit length (nL/mm) of **b** the ST fluid space, and **c** the OoC structure (including the OoC fluid spaces) in this case, in contrast to Fig. 5b), are compared between OCT and histology methods. The OCT results are plotted for the in vivo ( $N=5$ ) and PM states ( $N=3$ ) in terms of the mean  $\pm$  SD (blue lines), and for the in vivo state of an individual ear (#274L; magenta triangle). The histology results at a comparable location in the same animal (#274L, magenta diamond) and as the mean  $\pm$  SD ( $N=4$ , green diamond) are plotted to the right. **d** OoC cross-sectional areas are shown for the in vivo (blue;  $N=5$ ), 90-min-PM (yellow;  $N=3$ ), and histology

(green;  $N=4$ ) cases, with an added data point at  $800 \mu\text{m}$  (triangle) from Richter et al. (2000) based on a hemicochlea preparation from a zero-day-postnatal gerbil. **e–f** The measured OoC width (OoC<sub>w</sub>; **e**), along with histological results from Plassmann et al. (1987; light blue line; mean only;  $N=9$ ) and height (OoC<sub>h</sub>; **f**) of the OoC structure are plotted as functions of longitudinal position. The OCT mean  $\pm$  SD results are plotted for the in vivo state ( $N=5$ ; thick blue lines). Note that the gray diamonds mark the in vivo OCT and histology measurements from a location  $\sim 560 \mu\text{m}$  from the basal end of the cochlea. For the OCT method, both the mean  $\pm$  SD (thick blue lines) and results from an individual ear (#274L; thin magenta lines) are for the in vivo state. The histology measurements are plotted for an individual ear (#274L; thick magenta line) alongside the mean  $\pm$  SD ( $N=4$ ; green lines).

however, there was little change in the ST volume during the first 30 min after death (Fig. 9b, blue line). Thus, most of the shrinkage present in the ST volumes in the histological samples likely occurred during this chemical-perfusion stage of histological processing.

Figure 9c compares the volumes (per mm) of the OoC structure (now including the OoC fluid spaces), as measured using OCT and histology. The OCT results for the different states from in vivo to 90-min PM (mean  $\pm$  SD, blue line), and for one in vivo ear (magenta triangle), are shown alongside the mean  $\pm$  SD histology results ( $N=4$ ; green diamond with error bars concealed by the symbol), as well as the individual histology results from the same individual in vivo ear (magenta diamond). The OoC fluid spaces were hard to discern using the histological method, so no attempt was made to subtract those out. The mean

volume (per mm) of the OoC structure (with included fluid spaces) as measured in vivo with OCT (blue line) was about 4.9 times greater than that measured with histology (green diamond), and for the individual ear (magenta triangle vs. diamond), this ratio was about 4.7 times.

Figure 9d compares the mean  $\pm$  SE (standard error) of the OoC cross-sectional area as calculated from our in vivo (blue), 90-min-PM (yellow), and histology (green) measurements. The single data point (gray triangle) measured by (Richter et al. 2000) is from a hemicochlea preparation on a zero-day-postnatal gerbil at a location  $\sim 800 \mu\text{m}$  from the basal end of the cochlea. The in vivo cross-sectional OoC area at this location ( $18,430 \mu\text{m}^2$ ) is less than the 90-min-PM value ( $21,206 \mu\text{m}^2$ ), while the hemicochlea value ( $2,109 \mu\text{m}^2$ ) is much less than either of those values and is about

two times smaller than our histology value ( $5,118 \mu\text{m}^2$ ). This is consistent with the findings from several groups that gerbil hearing develops over an approximately three-week postnatal period during which the dimensions of the OoC structure increase significantly until postnatal day 12, after which the dimensions remain relatively constant (Finck et al. 1972; Müller 1996; Souter et al. 1997; Overstreet and Ruggero 1998). The volume of the OoC structure was found by integrating the measured cross-sectional areas over a length of 1–1.2 mm. These areas were also similarly greater when measured in vivo than when measured with histology (Fig. 9d).

Figures 9e, f compare  $\text{OoC}_W$  and  $\text{OoC}_H$ , respectively, as measured for the in vivo state vs. histology. Going from the basal end toward the apex, the histology-based average  $\text{OoC}_W$  increased rapidly (Fig. 9e, green line and error bars;  $N=4$ ). The OCT-based in vivo  $\text{OoC}_W$  values (Fig. 9e, blue line and error bars;  $N=5$ ) have a shallower slope than histology and are about 2 times larger than the corresponding histology values at the basal end (near 0.1 mm) but are slightly smaller at the more-apical end (near 0.9 mm). Furthermore, the OCT-based in vivo  $\text{OoC}_H$  values (Fig. 9f) are about 2–3 times larger than those from the corresponding histology measurements. For the individual ear, the differences between the OCT- and histology-based widths (Fig. 9e; thin and thick magenta lines, respectively) appear slightly greater than those between the average widths, but also with a steeper slope for histology. The histology-based volume (per mm) and dimensions of the OoC structures are smaller in comparison to the in vivo case (Fig. 9), and the in vivo case is typically smaller than the PM cases (Fig. 5e, f). Recall that for histology, the fixative was applied in vivo with cardiac perfusion. From this, we surmise that the decrease in dimensions in histology is not due to PM effects (Fig. 5e, f), but rather due to histological processing. The one caveat to this is that the tangential sectioning angle in histology could affect the measured width dimensions, which may explain the steeper slope in the histology width measurements. The tangential sectioning angle would not affect the height measurements. However, the height with histology is quite a bit smaller (Fig. 9f), which again argues that histological processing decreased the OoC dimensions. The reasons for the smaller width in the basal end are not clear, but this implies that the ridges used to define  $\text{OoC}_W$  might have moved closer toward each other during histological processing.

## DISCUSSION

We used a 905-nm-center-wavelength OCT system to collect 2D images and 3D volumes of the OoC fluid spaces and surrounding structures of the basal-turn hook region through the intact gerbil RWM. With an axial resolution of  $\sim 1.4 \mu\text{m}$  (in water) and a lateral resolution of  $\sim 1.95 \mu\text{m}$ , our system resolution is an improvement

by a factor of 2–8 in the axial direction and 5–8 in the lateral direction over 1310-nm-wavelength systems (Lee et al. 2015; Cooper et al. 2018; Fallah et al. 2019). With this improved capability, we were able to make morphometry measurements of important anatomical structures and fluid spaces of the intact living and PM cochlea with far better resolution than had been possible before.

For most mammalian cochleae, from base to apex the BM width increases, thickness decreases, and collagen-fiber volume fraction decreases gradually. A beam model incorporating these anatomical changes has been shown to result in a monotonically decreasing frequency-to-place cochlear map that describes the tonotopic organization of the cochlea for several species including guinea pig, human, and chinchilla (Von Békésy 1960; Steele and Taber 1979; Yoon et al. 2011).

The Mongolian gerbil used here, *Meriones unguiculatus*, is one of the species of the subfamily Gerbillinae from the Rodentia order of mammals. Of the five gerbil species studied, all are different from other mammals because of the pronounced arch in the  $\text{BM}_{PZ}$  (Fig. 1b–d), the lack of significant change in the BM width beyond the first 20% of the cochlear length, and the non-monotonic change in  $\text{BM}_{PZ}$  thickness along the cochlear length (Plassmann et al. 1987; Schweitzer et al. 1996; Kapuria et al. 2017). These characteristics have made understanding the gerbil cochlear map a challenge in light of the classical beam model that works well for other mammals but not gerbil. This was resolved by showing that in gerbil, the dominant factors that determine the cochlear map are the  $\text{BM}_{AZ}$  width, thickness, and collagen-fiber volume fraction (Kapuria et al. 2017; Xia et al. 2018). The  $\text{BM}_{PZ}$  arch with a gel-like substance inside the arch is thought to act like a stiff member with insignificant flexing. It is thought that, due to these anatomical factors, the asymmetric radial profile of BM motion tends to have a peak at the junction between the  $\text{BM}_{AZ}$  and  $\text{BM}_{PZ}$  regions (Homer et al. 2004). In previous model formulations, the  $\text{AZ}_W/\text{PZ}_W$  ratio was important for reproducing the radial profile of the BM (Kapuria et al. 2017; Xia et al. 2018). We set out to determine if the OoC widths and height change from in vivo to PM states in the gerbil cochlea, as this could have implications for understanding gerbil cochlear physiology and interpreting in vivo vibrometry measurements.

One of our present findings is that the width dimensions  $\text{AZ}_W$  and  $\text{PZ}_W$ , and thus  $\text{OoC}_W$ , change very little PM (Fig. 5c–e). Furthermore, the present  $\text{OoC}_W$  measurements are consistent with current (Fig. 9e) and previous (Plassmann et al. 1987) histological methods. Velocity measurements of the BM in vivo and PM also showed little change in the asymmetric radial profile of the BM (Homer et al. 2004), consistent with the present lack of changes in the  $\text{BM}_{AZ}$  and  $\text{BM}_{PZ}$  widths for the different animal states.

OoC<sub>H</sub> and the OoC area generally appear to be larger for 90-min PM than for in vivo, particularly basal to the 0.5-mm location (Figs. 5f and 9d), likely due to swelling, though this change was not deemed statistically significant. The measurements of OoC<sub>H</sub> and the OoC area are several times smaller with histological methods than with OCT methods (Fig. 9d, f), and thus those dimensions cannot be relied upon from histology. The present OCT-based results demonstrate that our histology-based understanding of in vivo OoC anatomy has been highly distorted in the high-frequency hook region. The present analysis suggests that the main cause of distortion in histology is likely due to processing effects and not due to PM effects.

In addition to in vivo structural morphometry measurements, we also measured the ISS and cortilymph fluid spaces. The ISS volume in vivo is bigger than the OT volume, but the ISS volume decreases and becomes comparable to the OT beyond 60-min PM (Fig. 8b, c). It is not clear what the PM decreases in the ISS dimensions are due to, but one possibility is swelling of the sulcus cells. However, this is likely to be a small effect. Another possibility is that, in the living cochlea, the ISS is pressurized by ISS-cell secretions, and that this internal pressure decreases 60 min after death, leading to a decreased ISS volume. The ToC and SN volumes did not change significantly PM (Fig. 7e, f), which is not surprising because

they are supported by the rigid outer and inner pillar cells.

One of the surprising findings is that the OT is larger than the ToC and SN by nearly a factor two (Fig. 7e–g). In classic OoC textbooks, the ToC is always prominently drawn and labeled, but the OT is rarely drawn and is typically missing (Echteler et al. 2012; Hubbard and Mountain 2012). This is likely because the OT is just barely visible in histology (e.g., Fig. 9a), and because of this, its importance for interpreting measurements and its effect on cochlear mechanics and modeling efforts have been absent from the literature.

In the region that contains the OT, there are several observed vibrational motions that are poorly understood, and it seems possible or even likely that a realistic appreciation of the OT and its surrounding anatomy is important for understanding these phenomena. The TCE and apical end of the nearby HCs (Fig. 10), sometimes called the “lateral compartment,” has a motion that can be 180° out of phase from BM motion in both active and passive cochleae (Gao et al. 2014). What makes the vibration pattern of this region differ from the BM has been a mystery. One reason for the great interest in the motion near the apical end of the OoC, such as lateral-compartment motion, is that the RL plays a prominent role in driving the OHC stereocilia with the phase required to allow OHC

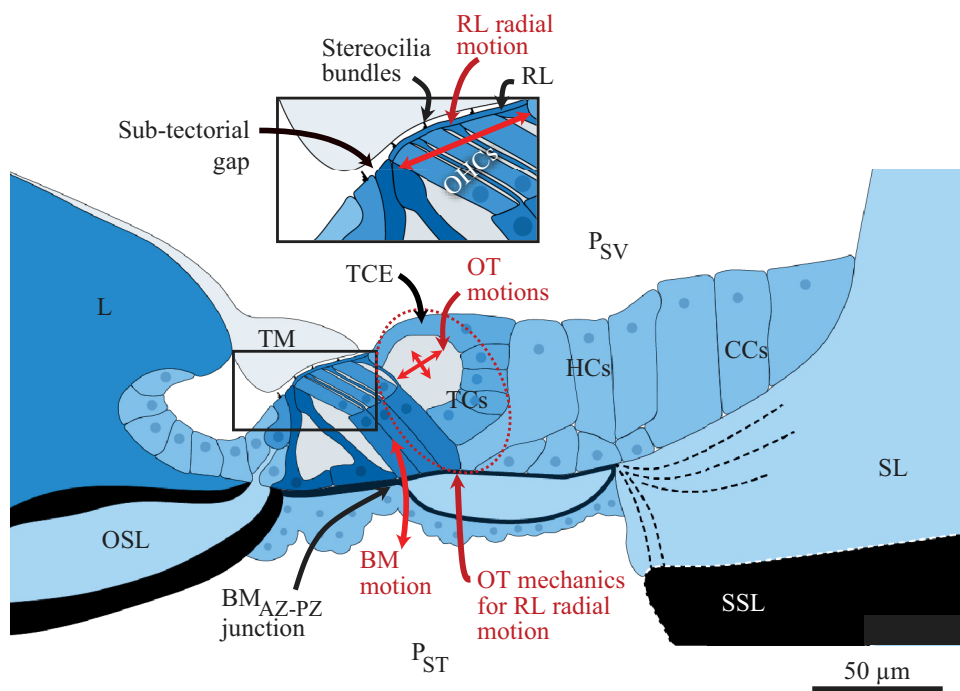


**FIG. 10.** Schematic of the OoC structures and fluid spaces, depicted here with the BM underneath, with red arrows indicating the proposed motions of the OT–RL-resonance hypothesis. The transverse motion of the BM from the traveling wave (red curved vertical arrow at the BM<sub>AZ-PZ</sub> junction) squeezes the OoC, and the resulting cochlear pressures and motions are postulated to affect

the OT fluid volume. Dynamic expansion and contraction of the OT fluid volume (cross-shaped arrows in the OT) may lead to radial vibration of the TCE, which through its attachment to the RL may then provide a mechanism for affecting the radial motion of the RL. The enlarged inset shows details of the sub-tectorial gap and stereocilia bundles between the TM and RL.

motility to amplify the traveling wave (Guinan 2020). Although it has been thought that a resonance in the radial motion of the TM is what drives the OHC stereocilia with the required phase for cochlear amplification (Gummer et al. 1996; Lukashkin et al. 2010; Sasmal and Grosh 2019; Nankali et al. 2020), recent OCT vibrational measurements have shown no TM radial resonance (Lee et al. 2016). Instead, the OHC-drive phase for cochlear amplification is produced by the RL vibrating out-of-phase from the BM (Lee et al. 2016; Guinan 2020). Again, it remains a mystery how this RL-vibration phase comes about, and to our knowledge no mechanism has been published that could explain how such a shift in the RL phase could arise. We hypothesize that the large OT space, through its effect on fluid dynamics within the OoC, plays an important role in producing these mysterious vibration patterns.

In our hypothesis, the transverse motion of the BM in a traveling wave (Fig. 10, red curved vertical arrow) squeezes the OoC and produces pulsatile motion of the cell walls surrounding the OT fluid space (Fig. 10). Depending on the wall stiffness, fluid mass, and steady-streaming Reynolds number, the wall motion may excite resonance modes (Secomb 1978). We hypothesize that OT resonance modes can induce radial and transverse motions of the TCs at the apical region of the OT that vibrate the TCE attached to the outer edge of the RL and thus provide a mechanism for radial motion of the RL (Fig. 10, red dotted ellipse). This “OT–RL-resonance” would be present for both active and passive mechanics and may be amplified by the active pumping of fluid into the OT by the OHCs. An alternative way that OT motion may be coupled to RL motion is through fluid motion in the intra-OoC fluid spaces. Details of this hypothesis are lacking, but its essence is that the large OT fluid space must have a substantial effect on cochlear mechanics and may be instrumental in producing an OHC drive at the correct phase to produce cochlear amplification. A related possibility is that the OT might form a low-impedance boundary for the third row of OHCs such that they can vibrate more than the other two rows due to this lower OT fluid impedance. Testing these hypotheses will require new physiological measurements, improved OCT methods, and further developments in FE modeling.

## ACKNOWLEDGEMENTS

We thank the MEE Otopathology staff and Anbuselvan Dharmarajan for preparing histology slides; Michael E. Ravicz and John J. Guinan, Jr., for technical support and assistance with cochlear-sensitivity measurements; Kevin N. O’Connor, Heidi H. Nakajima, John J. Guinan, Jr., and Rachel Chen for editing assistance; M. Charles Liberman and Jennifer T. O’Malley for helpful discussions regarding the histology measurements; and Andrew A. Tubelli for

the OoC-structure drawings (Figs. 1b, d and 10). We thank Kovid T. Puria for help with statistical analyses.

*Author Contribution* N.H.C. and S.P. conceived of and designed the project. N.H.C. developed the VibOCT software, conducted the experiments, and reconstructed the 3D OCT volumes. H.W. performed the segmentation and analysis of the 3D volumes from OCT and histology. S.P., N.H.C., and H.W. wrote and edited the manuscript, and S.P. supervised the project.

*Funding* This work was supported in part by Grant R01 DC07910 from the National Institute on Deafness and Other Communication Disorders (NIDCD) of the NIH, and the Amelia Peabody Charitable Fund.

*Data Availability* All data needed to evaluate the conclusions in the paper are present in the paper. Additional data related to this paper may be requested from the authors.

## Declarations

*Conflict of Interest* The authors declare no competing interests.

## REFERENCES

- COOPER NP, VAVAKOU A, VAN DER HEIJDEN M (2018) Vibration hot-spots reveal longitudinal funneling of sound-evoked motion in the mammalian cochlea. *Nat Commun* 9:3054. <https://doi.org/10.1038/s41467-018-05483-z>
- ECHTELER SM, FAY RR, POPPER AN (2012) Structure of the mammalian cochlea. In: *Comparative Hearing: Mammals*. Springer Science & Business Media pp 134–171
- EDGE RM, EVANS BN, PEARCE M ET AL (1998) Morphology of the unfixed cochlea. *Hear Res* 124:1–16
- FALLAH E, STRIMBU CE, OLSON ES (2019) Nonlinearity and amplification in cochlear responses to single and multi-tone stimuli. *Hear Res* 377:271–281. <https://doi.org/10.1016/j.heares.2019.04.001>
- FINCK A, SCHNECK CD, HARTMAN AF (1972) Development of cochlear function in the neonate Mongolian gerbil (*Meriones unguiculatus*). *J Comp Physiol Psychol* 78:375
- GAO SS, WANG R, RAPHAEL PD ET AL (2014) Vibration of the organ of Corti within the cochlear apex in mice. *J Neurophysiol* 112:1192–1204. <https://doi.org/10.1152/jn.00306.2014>
- GUINAN JJ (2020) The interplay of organ-of-Corti vibrational modes, not tectorial-membrane resonance, sets outer-hair-cell stereocilia phase to produce cochlear amplification. *Hear Res* 395:108040. <https://doi.org/10.1016/j.heares.2020.108040>
- GUMMER AW, HEMMERT W, ZENNER HP (1996) Resonant tectorial membrane motion in the inner ear: its crucial role in frequency tuning. *Proc Natl Acad Sci* 93:8727–8732. <https://doi.org/10.1073/pnas.93.16.8727>
- HARDIE NA, MACDONALD G, RUBEL EW (2004) A new method for imaging and 3D reconstruction of mammalian cochlea by fluorescent confocal microscopy. *Brain Res* 1000:200–210. <https://doi.org/10.1016/j.brainres.2003.10.071>
- HENSON MM, JENKINS DB, HENSON OW (1983) Sustentacular cells of the organ of Corti — the tectal cells of the outer tunnel. *Hear Res* 10:153–166. [https://doi.org/10.1016/0378-5955\(83\)90051-5](https://doi.org/10.1016/0378-5955(83)90051-5)
- HOMER M, CHAMPNEYS A, HUNT G, COOPER N (2004) Mathematical modeling of the radial profile of basilar membrane vibrations in the inner ear. *The Journal of the Acoustical Society of America* 116:1025–1034. <https://doi.org/10.1121/1.1771571>



- HU X, EVANS BN, DALLOS P (1999) Direct visualization of organ of Corti kinematics in a hemicochlea. *J Neurophysiol* 82:2798–2807
- HUANG D, SWANSON EA, LIN CP ET AL (1991) Optical coherence tomography. *Science* 254:1178–1181
- HUBBARD AE, MOUNTAIN DC (2012) Analysis and synthesis of cochlea mechanical function using models. In: *Auditory computation*. Springer Science & Business Media pp 62–120
- IVER JS, BATTS SA, CHU KK ET AL (2016) Micro-optical coherence tomography of the mammalian cochlea. *Sci Rep* 6:33288. <https://doi.org/10.1038/srep33288>
- JACKSON RP (2014) Rotational axes and lever arms for the middle-ear ossicles of several land mammals. Dissertation, Stanford University
- KAPURIA S, STEELE CR, PURIA S (2017) Unraveling the mystery of hearing in gerbil and other rodents with an arch-beam model of the basilar membrane. *Sci Rep* 7:228. <https://doi.org/10.1038/s41598-017-00114-x>
- LEE HY, RAPHAEL PD, PARK J ET AL (2015) Noninvasive in vivo imaging reveals differences between tectorial membrane and basilar membrane traveling waves in the mouse cochlea. *Proc Natl Acad Sci* 112:3128–3133. <https://doi.org/10.1073/pnas.1500038112>
- LEE HY, RAPHAEL PD, XIA A ET AL (2016) Two-dimensional cochlear micromechanics measured in vivo demonstrate radial tuning within the mouse organ of Corti. *J Neurosci* 36:8160–8173. <https://doi.org/10.1523/JNEUROSCI.1157-16.2016>
- LIM DJ, ANNIKO M (1985) Developmental morphology of the mouse inner ear: a scanning electron microscopic observation. *Acta Otolaryngol* 99:5–69. <https://doi.org/10.3109/00016488509121766>
- LUKASHKIN AN, RICHARDSON GP, RUSSELL IJ (2010) Multiple roles for the tectorial membrane in the active cochlea. *Hear Res* 266:26–35. <https://doi.org/10.1016/j.heares.2009.10.005>
- MEENDERINK SWF, SHERA CA, VALERO MD ET AL (2019) Morphological immaturity of the neonatal organ of Corti and associated structures in humans. *J Assoc Res Otolaryngol* 20:461–474. <https://doi.org/10.1007/s10162-019-00734-2>
- MERCHANT SN, NADOL JB (2010) *Schuknecht's pathology of the ear*, Third Edition. People's Medical Publishing House
- MÜLLER M (1996) The cochlear place-frequency map of the adult and developing Mongolian gerbil. *Hear Res* 94:148–156
- NANKALI A, WANG Y, STRIMBU CE ET AL (2020) A role for tectorial membrane mechanics in activating the cochlear amplifier. *Sci Rep* 10:17620. <https://doi.org/10.1038/s41598-020-73873-9>
- O'MALLEY JT, MERCHANT SN, BURGESS BJ ET AL (2009) Effects of fixative and embedding medium on morphology and immunostaining of the cochlea. *Audiol Neurotol* 14:78–87. <https://doi.org/10.1159/000158536>
- OVERSTREET EH, RUGGERO MA (1998) Basilar membrane mechanics at the hook region of the Mongolian gerbil cochlea. *Assoc Res Otolaryngol mid-Winter Meet Abst* 21:181
- PETERSON LC, BOGERT BP (1950) Erratum: a dynamical theory of the cochlea. *J Acoust Soc* 22:640–640. <https://doi.org/10.1121/1.1906668>
- PLASSMANN W, PEETZ W, SCHMIDT M (1987) The Cochlea in Gerbilline Rodents *BBE* 30:82–102. <https://doi.org/10.1159/000118639>
- RICHTER C-P, EDGE R, HE DZZ, DALLOS P (2000) Development of the gerbil inner ear observed in the hemicochlea. *J Assoc Res Otolaryngol* 1:195–210. <https://doi.org/10.1007/s101620010019>
- SASMAL A, GROSH K (2019) Unified cochlear model for low- and high-frequency mammalian hearing. *Proc Natl Acad Sci* 116:13983–13988. <https://doi.org/10.1073/pnas.1900695116>
- SCHWEITZER L, LUTZ C, HOBBS M, WEAVER SP (1996) Anatomical correlates of the passive properties underlying the developmental shift in the frequency map of the mammalian cochlea. *Hear Res* 97:84–94. [https://doi.org/10.1016/S0378-5955\(96\)80010-4](https://doi.org/10.1016/S0378-5955(96)80010-4)
- SECOMB TW (1978) Flow in a channel with pulsating walls. *J Fluid Mech* 88:273–288. <https://doi.org/10.1017/S0022112078002104>
- SOUTER M, NEVILL G, FORGE A (1995) Postnatal development of membrane specialisations of gerbil outer hair cells. *Hear Res* 91:43–62. [https://doi.org/10.1016/0378-5955\(95\)00163-8](https://doi.org/10.1016/0378-5955(95)00163-8)
- SOUTER M, NEVILL G, FORGE A (1997) Postnatal maturation of the organ of Corti in gerbils: morphology and physiological responses. *J Comp Neurol* 386:635–651
- SPICER SS, SCHULTE BA (1994) Ultrastructural differentiation of the first Hensen cell in the gerbil cochlea as a distinct cell type. *Anat Rec* 240:149–156. <https://doi.org/10.1002/ar.1092400202>
- SPICER SS, SMYTHE N, SCHULTE BA (2003) Ultrastructure indicative of ion transport in tectal, Deiters, and tunnel cells: differences between gerbil and chinchilla basal and apical cochlea. *Anat Rec* 271A:342–359. <https://doi.org/10.1002/ar.a.10041>
- STEELE CR, TABER LA (1979) Comparison of WKB calculations and experimental results for three-dimensional cochlear models. *J Acoust Soc* 65:1007–1018. <https://doi.org/10.1121/1.382570>
- VON BÉKÉSY G (1960) *Experiments in hearing*. McGraw, New York
- XIA A, UDAGAWA T, RAPHAEL PD ET AL (2018) Basilar membrane vibration after targeted removal of the third row of OHCs and Deiters cells. *St Catharines, Canada* p 020004. <https://doi.org/10.1063/1.5038451>
- YOON Y-J, STEELE CR, PURIA S (2011) Feed-forward and feed-backward amplification model from cochlear cytoarchitecture: an interspecies comparison. *Biophys J* 100:1–10. <https://doi.org/10.1016/j.bpj.2010.11.039>

*Publisher's Note* Springer Nature remains neutral with regard to jurisdictional claims in published maps and institutional affiliations.